Inorganic Chemistry
ARTICLE
pubs.acs.org/IC

Size- and Shape-Selective Isostructural Microporous Metal−Organic Frameworks with Different Effective Aperture Sizes

Xinfang Liu,[†,‡] Minhak Oh,[†] and Myoung Soo Lah[*,†]

[†]Interdisciplinary School of Green Energy, Ulsan National Institute of Science & Technology, Ulsan, 689-798, Korea
[‡]Department of Chemistry and Applied Chemistry, College of Science and Technology, Hanyang University, Ansan, Kyunggi-do 426-791, Korea

Supporting Information

ABSTRACT: Two isostructural metal−organic frameworks (MOFs) having micropores of the same "static aperture size" but different "effective aperture size" have been prepared using 5-(pyridin-3-ylethynyl)isophthalic acid as a ligand having two different types of functional units, an isophthalate (iph) unit and a pyridyl unit, simultaneously in a single ligand. The combination of iph unit and Cu (or Zn) ion led to two-dimensional layers of Kagomé (**kgm**) net topology, the layers being further pillared by the internal auxiliary pyridyl unit to form a three-dimensional microporous framework having two different types of cage-like pores, cage A and cage B, with different aperture sizes and shapes. (1) The MOFs can distinguish the adsorbates (N_2/Ar) not based on the widely used kinetic diameters of the adsorbates but based on the minimum diameters of the adsorbates, which are more shape dependent. While cage A with a sufficiently large aperture size compared with the size of the adsorbates does not show any size selectivity, cage B with an approximate size match between the adsorbates and the pore apertures shows shape selectivity for the adsorbates. The smaller but spherically shaped Ar atom is not allowed into the pore with the oval-shaped aperture; however, the larger linear N_2 molecule is allowed into the pore with the oval-shaped aperture. (2) Even though the two isostructural MOFs have the same static aperture size of cage B, they show different size selectivity for the adsorbates based on the effective aperture size, which reflects the different extents of the framework flexibility.

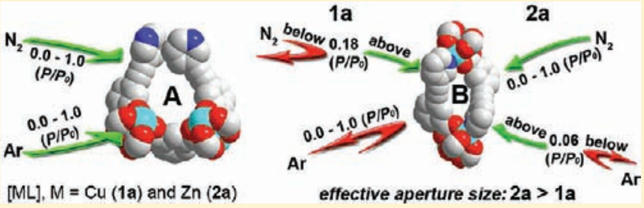

INTRODUCTION

Traditional porous materials, such as inorganic zeolites, have been studied extensively as adsorbents and have achieved considerable success for selective gas adsorption and separation.[1] However, it is not easy to control the selectivity of the zeolites because of the difficulties in modulating the pore characteristics. In contrast to traditional porous materials, metal−organic frameworks (MOFs) with inherent diversities in their structures and properties could be utilized for diverse selective gas separation and purification processes.[2] These diversities prompt the need to understand better the factors affecting gas adsorption and separation phenomena, for example, the adsorbate's size and shape, the adsorbate's chemical nature, the pore size and shape of the adsorbents, the chemical nature of the adsorbents, the flexibility of the adsorbents, and so on. For breathing or flexible MOFs, an adsorbate dependent pressure-triggered[3,4] or temperature-triggered[5] gate opening could result in selectivity for guest adsorption. For rigid MOFs, size-exclusive gating is a simple but dominant factor for adsorbate selectivity.[6] Size exclusive selectivity can be explained mainly based on a simple comparison of the size of adsorbates such as the widely used kinetic diameter (KD)[7] and the aperture sizes of the pores estimated from the crystal structures. The adsorbates of smaller KDs are allowed to pass through the aperture, while the adsorbates with larger KDs are not. However, the KD assumes that the adsorbate is spherical, and the adsorbate's shape has not been taken into account. For a nonspherical adsorbate, the minimum dimension (MIN-2)[8] of the adsorbate might be more appropriate for determining whether the adsorbate can pass through an aperture or not.[9] Even for MOF having a so-called "rigid" pore, the pore is not static and the aperture dimensions vary depending on the different extents of the pore flexibilities due to the different thermal motions of the constituent atoms. The size-exclusive principle of the adsorbents is not dependent on the "static aperture size", the aperture size calculated based on the crystal structure, but depends on the "effective aperture size", the maximum allowed aperture size estimated considering the thermal vibration of the constituent atoms of the aperture.[10]

An isophthalate (iph) unit is used for the construction of metal−organic polyhedra (MOPs),[11] two-dimensional (2-D) layer of square (**sql**) net topology[12] or Kagomé (**kgm**) net topology[13] based on a square paddle-wheel secondary building unit (SBU). In the presence of an additional auxiliary interlinking ligand, the MOPs can be further interconnected to generate a three-dimensional (3-D) porous MOFs based on the MOPs.[14]

Received: February 17, 2011
Published: May 09, 2011

dx.doi.org/10.1021/ic200328q | *Inorg. Chem.* 2011, 50, 5044–5053

Scheme 1. The Ligand 5-(Pyridin-3-ylethynyl)isophthalic Acid (H_2L)

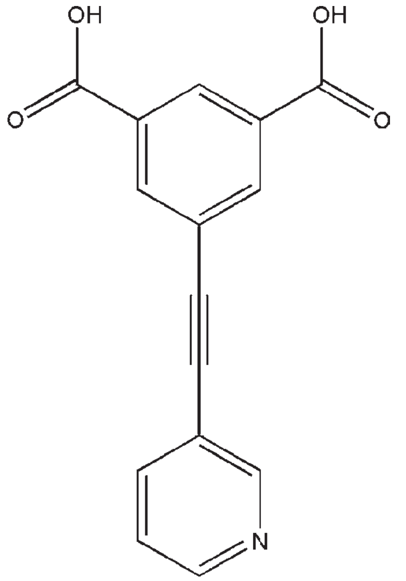

Several examples of the pillaring of the 2-D layers having a linear dicarboxylate unit such as a terphthalate group using additional auxiliary linkers have been reported.[15] Recently, two Cu-based MOFs have been reported using the ligands containing both the iph unit and either pyridyl or tetrazole group directly attached to the iph unit as an auxiliary internal interlinking group.[16] Both frameworks are 3-D networks based on a 2-D **sql** network pillared by the auxiliary internal interlinking group, pyridyl or tetrazole unit.

We report herein the preparation of two size- and shape-selective isostructural MOFs having micropores of the same "static aperture size" but of different effective aperture size. The MOFs have been prepared via hydrosolvothermal reaction of Cu(II) ion or solvothermal reaction of Zn(II) ion as a metal source and 5-(pyridin-3-ylethynyl)isophthalic acid (H_2L) as a ligand (Scheme 1). The ligand has two different functional units simultaneously in a single ligand, an iph unit and the pyridyl unit as an auxiliary internal connecting residue, where the two units are interconnected via C−C triple bond of some degree of rotational freedom. The combination of the iph unit and Cu (or Zn) ion led to 2-D layers of a **kgm** net topology based on square paddle-wheel as an SBU, and the layers were further pillared by the pyridyl unit of the ligand to form a 3-D microporous framework having two different types of cage-like pores with different static aperture sizes and shapes. The size- and shape-selective gas sorption characteristics of the two isostructural MOFs as well as the effect of the framework's flexibility on the effective aperture size of the pores have been investigated.

■ EXPERIMENTAL SECTION

General Procedures. All reagents were purchased from commercial sources and were used without further purification. Elemental analyses were conducted at the Elemental Analysis Laboratory of the Korean Basic Science Institute, Korea. Mass spectral data were obtained on a Jeol JMS 700 high-resolution mass spectrometer (HRMS) at the Korea Basic Science Institute (Daegu). FT−IR spectra were recorded as KBr pellets with a Varian 1000 FT−IR spectrophotometer ($4000-400\ \mathrm{cm}^{-1}$). Thermogravimetric analyses (TGA) were performed using a TA Instruments (Q200, USA) with a heating rate of $10\ °\mathrm{C\ min}^{-1}$ between ambient temperature and 500 °C in air. Nuclear magnetic resonance (NMR) spectra were recorded on a Varian-500 spectrometer. Powder X-ray diffraction (PXRD) data were recorded using a Rigaku D/M 2200T automated diffractometer at room temperature, with a step size of 0.02° in 2θ angle. The variable temperature PXRD (VT-PXRD) measurements were carried out in air, using a Bruker D8 Advance system. Samples were gradually heated from room temperature, with a holding time of at least 30 min at each temperature. Simulated PXRD patterns were calculated with the Material Studio program[17] using the single crystal data.

Preparation of 5-(Pyridin-3-ylethynyl)isophthalic Acid Dimethyl Ester. A solution of triethylamine (30 mL) in anhydrous tetrahydrofuran (THF) (60 mL) was degassed by bubbling dry N_2 through it for 30 min. To this was added dimethyl-5-iodoisophthalate (3.201 g, 10.00 mmol), dichlorobis(triphenylphosphine)palladium(II) (0.175 g, 0.249 mmol), and copper(I) iodide (0.145 g, 0.761 mmol). The resulting mixture was stirred at room temperature for 30 min, and then a solution of 3-ethynylpyridine (1.031 g, 10.00 mmol) in anhydrous THF (15 mL) was added dropwise over about 20 min, while bubbling. The reaction mixture was stirred for an additional 12 h at room temperature. The light-orange precipitate formed was separated by filtration and the filtrate was dissolved in 50 mL of dichloromethane. The organic phase was washed three times with 100 mL of water and then dried over anhydrous $MgSO_4$. The volatiles were removed by evaporation under reduced pressure, and the solid residue was freeze-dried. Yield = 1.89 g, 64.1%. HRMS (FAB) m/z calcd for $C_{17}H_{14}NO_4$ $[M + 1]^+$ 296.0923, found 296.0923; ^1H NMR spectrum (500 MHz, $CDCl_3$, δ ppm) 8.79 (s, 1H, Py-H), 8.66 (s, 1H, Ar-H), 8.60 (d, 1H, Py-H), 8.36 (s, 2H, Ar-H), 7.84 (d, 1H, Py-H), 7.32 (dd, 1H, Py-H), 3.98 (s, 6H, -CH_3); ^{13}C NMR spectrum (125 MHz, $CDCl_3$, δ ppm): 165.67, 152.55, 149.33, 138.81, 136.75, 131.27, 130.74, 123.81, 123.35, 119.91, 90.70, 87.92, 52.81; IR spectrum (KBr, cm^{-1}): 3007(w), 2954(w), 1727(s), 1598(w), 1561(w), 1477(m), 1437(s), 1422(w), 1406(w), 1352(m), 1276(s), 1246(s), 1195(m), 1157(m), 1121(w), 1104(m), 1044(w), 1022(w), 998(m), 912(w), 875(w), 802(m), 753(s), 723(m), 697(m), 670(w), 626(w), 558(w).

Preparation of 5-(Pyridin-3-ylethynyl)isophthalic Acid (H_2L). A sample of potassium hydroxide (5.611 g, 100.0 mmol) was dissolved in 100 mL of methanol. To this was added 5-(pyridin-3-ylethynyl)isophthalic acid dimethyl ester (1.480 g, 5.017 mmol), after which the solution was stirred for 8 h at 80 °C. The volatiles were removed by evaporation under reduced pressure. The residue dissolved in 100 mL of water was acidified to pH ∼2−3 using 1.0 M HCl and stirred for 5 h. The pale gray precipitate was separated by filtration, washed with water, and freeze-dried. Yield = 1.28 g, 95.2%. HRMS (FAB) m/z calcd for $C_{15}H_{10}NO_4$ $[M + 1]^+$ 269.0610, found 269.0656; ^1H NMR spectrum (500 MHz, DMSO-d_6, δ ppm) 13.56 (s, 2H, −COOH), 8.83 (s, 1H, Py-H), 8.62 (d, 1H, Py-H), 8.46 (s, 1H, Ar-H), 8.29 (s, 2H, Ar-H), 8.06 (d, 1H, Py-H), 7.49 (dd, 1H, Py-H); ^{13}C NMR spectrum (125 MHz, DMSO-d_6, δ ppm): 165.77 (C12), 151.90 (C1), 149.45 (C2), 138.85 (C4), 135.67 (C9), 132.10 (C11), 130.08 (C10), 123.66 (C3), 122.83 (C8), 118.84 (C5), 90.27 (C7), 87.78 (C6) (see Scheme S1 for the atom labeling of the ligand); IR spectrum (KBr, cm^{-1}): 3082(s), 2552(w), 2221(w) ($-\underline{C}{\equiv}\underline{C}-$), 1716(s) (carboxyl $-\underline{C{=}O}$), 1598(w), 1567(w), 1476(m), 1435(m), 1408(m), 1340(m), 1320(m), 1254(s), 1236(s), 1168(s), 1120(m), 1053(m), 915(m), 814(m), 760(s), 690(m), 676(m), 597(m), 552(m), 510(m).

Preparation of [CuL]·xDMF·yH_2O, 1 (where x and y are the numbers of solvent molecules). A solution of $Cu(NO_3)_2 \cdot 2.5H_2O$ (0.0230 g, 0.0989 mmol) in 0.10 mL of H_2O was mixed with the H_2L (0.0027 g, 0.010 mmol) in 1.00 mL of *N,N*-dimethylformamide (DMF). To this was added 0.10 mL of HCl (concentrated HCl/H_2O (v/v): 1/5), with stirring. The mixture was sealed in a Pyrex tube and heated to 85 °C for 12 h. The blue hexagonal plate crystals obtained were filtered

Table 1. Crystal Data and Structure Refinements for 1, 1a, 2, and 2a

		1	1a	2	2a
empirical formula		$C_{15}H_7NO_4Cu$	$C_{15}H_7NO_4Cu$	$C_{15}H_7NO_4Zn$	$C_{15}H_7NO_4Zn$
formula weight		328.76	328.76	330.59	330.59
space group		$R\bar{3}c$	$R\bar{3}c$	$R\bar{3}m$	$R\bar{3}m$
unit cell dimensions (Å)	*a*	18.249(3)	18.218(3)	18.628(3)	18.667(3)
	b	18.249(3)	18.218(3)	18.628(3)	18.667(3)
	c	72.569(15)	72.761(15)	36.435(7)	36.398(7)
volume (Å^3)		20928(6)	20913(6)	10950(3)	10984(3)
Z		36	36	18	18
D_{calcd} (g cm^{-3})		0.939	0.940	0.902	0.900
μ (mm^{-1})		0.947	0.948	1.017	1.014
F(000)		5940	5940	2988	2988
total/unique reflections		68489, 8898	68384, 8891	28992, 2987	34878, 3051
R_{int}		0.1105	0.0913	0.0749	0.0405
R_1, wR_2		0.0730, 0.1922	0.0524, 0.1279	0.0628, 0.1849	0.0581, 0.2239
goodness-of-fit		1.053	1.074	1.128	1.088
difference Fourier map, max, min (e·Å^{-3})		3.246, −1.885	1.024, −1.103	0.647, −0.460	1.087, −0.381

and washed with DMF. IR spectrum (KBr, cm^{-1}): 3412(m), 3070(m), 2962(m), 2216(w) ($-\underline{C}\equiv\underline{C}-$), 1648(s) (amide $-\underline{C}=\underline{O}$ in DMF), 1575(s) ($-COO_s$), 1482(w), 1424(s), 1374(s) ($-\underline{COO_a}$), 1261(s), 1188(w), 1098(s), 1028(m), 917(w), 864(w), 805(s), 774(m), 730(m), 698(m), 555(w), 490(w). Note: The extent to which the solvent molecules occupy the pores of **1** varies depending on the exposure time of the sample to air. The activated sample, **1a**, was prepared by repeatedly soaking and desolvating **1** in DMF, then vacuum-drying at 200 °C overnight to yield 0.0018 g of product (54.2%, based on the ligand). Elemental analysis of the sample of air-exposed **1a** was carried out. Calcd for [CuL], ($C_{15}H_7NO_4Cu$, fw = 328.77): C 54.80, H 2.15, N 4.26%; found: C 54.91, H 2.25, N 4.15%. This EA result is consistent with the TGA data of **1a** (Figure S1, Supporting Information).

Preparation of [ZnL]·xDEF·yH$_2$O, 2 (where x and y are the number of solvent molecules). A solution of $Zn(NO_3)_2 \cdot 6H_2O$ (0.0060 g, 0.0202 mmol) and H_2L (0.0027 g, 0.0101 mmol) in 1.00 mL *N,N*-diethylformamide (DEF) was sealed in a Pyrex tube and heated to 85 °C for 12 h. The colorless block crystals obtained were filtered and washed with DEF. IR spectrum (KBr, cm^{-1}): 3415(m), 3075(m), 2967(m), 2220(w) ($-\underline{C}\equiv\underline{C}-$), 1655(s) (amide $-\underline{C}=\underline{O}$ in DMF), 1586(s) ($-COO_s$), 1482(w), 1430(s), 1374(s) ($-\underline{COO_a}$), 1261(s), 1191(w), 1103(s), 1030(m), 918(w), 864(w), 803(s), 776(m), 723(m), 697(m), 550(w), 455(w). Note: The extent to which the solvent molecules occupy the pore again varies depending on the exposure time of the sample to air. **2** was dried in air to yield 0.0016 g of product (35.3%, based on the ligand). Elemental analysis of the sample of air-dried **2** was carried out. Calcd for [ZnL]·DEF·H$_2$O, ($C_{20}H_{20}N_2O_6Zn$, fw = 449.77): C 53.41, H 4.48, N 6.23%; found: C 53.51, H 4.52, N 6.52%. This EA result is consistent with the TGA data of **2** (Figure S1, Supporting Information). The activated sample, **2a**, was prepared by repeatedly soaking and desolvating **2** in DEF, then vacuum-drying at 150 °C overnight to yield 0.0011 g of product (32.9%, based on the ligand).

Crystallographic Data Collection and Refinement of Structures. The crystals of **1**, **1a**, and **2** were coated with paratone oil and the diffraction data were measured at 99 (or 100) K with synchrotron radiation (λ = 0.75000 Å) on a 6BMXW ADSC Quantum-210 detector with a Pt-coated Si double crystal monochromator at the Pohang Accelerator Laboratory, Korea. The ADSC Quantum-210 ADX program[18] was used for data collection; HKL2000 (Ver. 0.98.698a)[19] was used for cell refinement, reduction, and absorption correction. A crystal of **2a** was coated with paratone oil and the diffraction data were measured at 173 K with Mo Kα radiation on an X-ray diffraction camera system using an imaging plate equipped with a graphite crystal incident beam monochromator. The RapidAuto software[20] was used for data collection and processing.

All the structures were solved by direct methods and refined by full-matrix least-squares calculations with the SHELXTL software package.[21] In the structure of **1**, one copper cation, one ligand, a DMF molecule of 0.357 site occupancy, and a water molecule of 0.418 site occupancy were observed as an asymmetric unit. All non-hydrogen atoms except the atoms of the solvent molecules were refined anisotropically; the atoms of the solvent molecules were refined isotropically. The hydrogen atoms attached to the ligand and the solvent DMF molecule were assigned isotropic displacement coefficients U(H) = 1.2U (or 1.5U) (C) and their coordinates were allowed to ride on their respective atoms. The hydrogen atoms of the solvent water molecule were not included in the least-squares refinement. The distances and the angles in the DMF molecule were restrained using DFIX and DANG during the least-squares refinement because of poor geometry. The refinement converged to R_1 = 0.0921 and wR_2 = 0.2574 for 7130 reflections with $I > 2\sigma(I)$. Structure refinement after modification of the data for the solvent molecules with the SQUEEZE routine of PLATON[22] (after removing solvent molecules, 11450 Å^3, 54.7% of the crystal volume) led to better refinement and data convergence. Refinement of the structure converged at a final R_1 = 0.0730 and wR_2 = 0.1922 for 7242 reflections with $I > 2\sigma(I)$; R_1 = 0.0875 and wR_2 = 0.2013 for all reflections. The largest differences in peak and hole were 3.246 and −1.885 e·Å^{-3}, respectively.

Crystal **1a** was prepared by activating crystal **1** with vacuum-drying at 200 °C overnight. In the structure of **1a**, one copper cation and one ligand were observed as an asymmetric unit. All non-hydrogen atoms were refined anisotropically; only the hydrogen atoms attached to the ligand were assigned isotropic displacement coefficients U(H) = 1.2U (C) and their coordinates were allowed to ride on their respective atoms. The refinement of the structure converged at a final R_1 = 0.0524 and wR_2 = 0.1279 for 6684 reflections with $I > 2\sigma(I)$; R_1 = 0.0802 and wR_2 = 0.1412 for all reflections. The largest differences in peak and hole were 1.024 and −1.013 e·Å^{-3}, respectively.

In the structure of **2**, one zinc cation and one ligand on the crystallographic mirror plane and two water molecules on the crystallographic $3m$ symmetry sites were observed as an asymmetric unit. The pyridyl group of the ligand was statistically disordered. All non-hydrogen atoms were refined anisotropically; only the hydrogen atoms attached to the

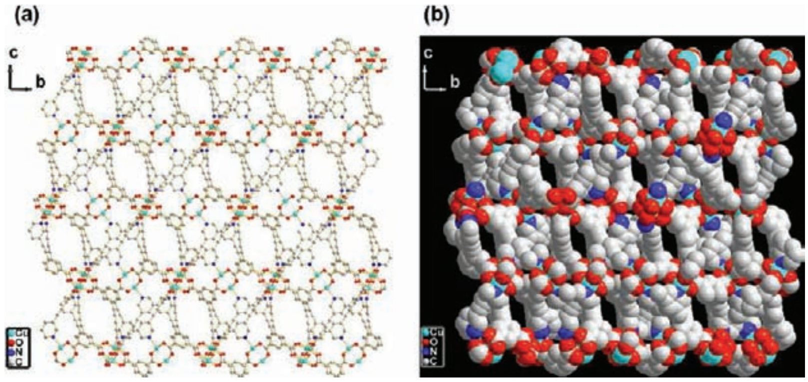

Figure 1. A packing diagram of **1**, (a) ball-and-stick and (b) space-filling drawings. All hydrogen atoms and guest molecules are omitted for clarity.

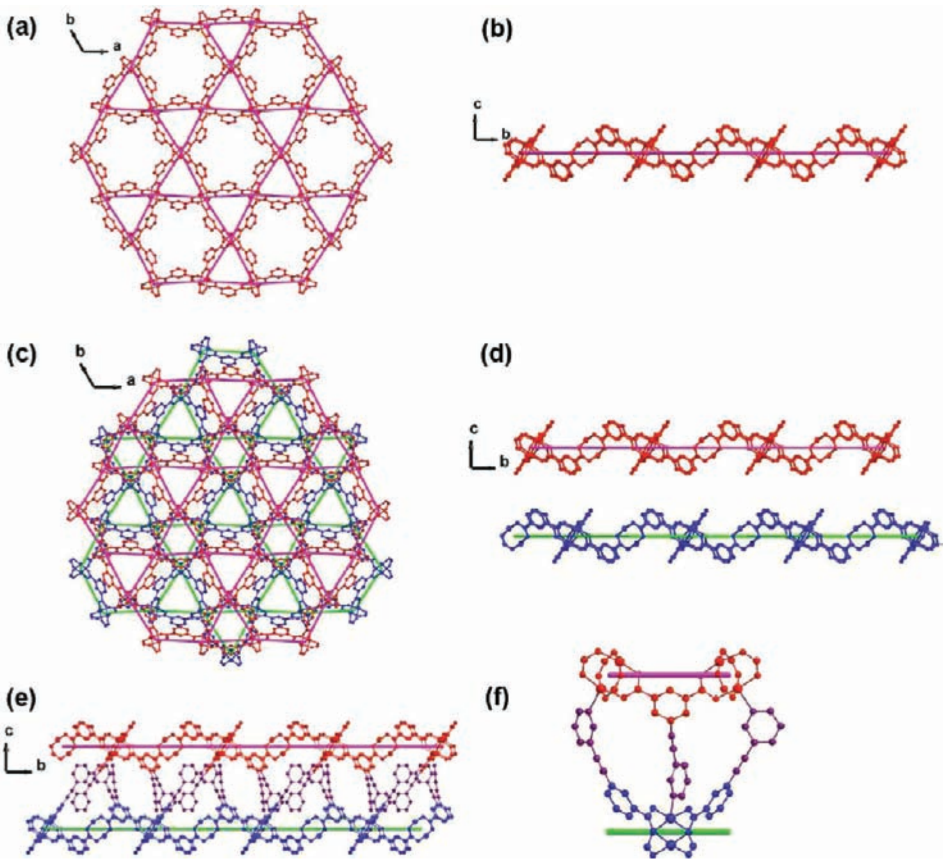

Figure 2. Views of the Kagomé 2-D layers based on the paddle-wheel SBU, (a) a view of a 2-D layer along the crystallographic *c*-axis; (b) a view of the 2-D layer along the crystallographic *a*-axis; (c) a view of the two adjacent 2-D layers along the crystallographic *c*-axis; (d) a view of the two adjacent 2-D layers along the crystallographic *a*-axis; (e) a view showing the pillaring between the two adjacent 2-D layers via the internal auxiliary pyridyl units; (f) a view showing the coordination of pyridyl groups to the fifth coordination site of the metal centers of the paddle-wheel SBUs of the neighboring layers. The pink and the green sticks are schematic representations of the 2-D Kagomé layers.

ligand except one hydrogen atom of the statistically disordered pyridyl group were assigned isotropic displacement coefficients U(H) = 1.2U (C) and their coordinates were allowed to ride on their respective atoms. The hydrogen atoms of the solvent water molecules and one hydrogen atom of the disordered pyridyl group were not included in the least-squares refinement. The refinement converged to $R_1 = 0.0790$ and $wR_2 = 0.2310$ for 2399 reflections with $I > 2\sigma(I)$. Structure refinement after modification of the data for the solvent molecules with the SQUEEZE routine of PLATON (after removing solvent molecules, 5931 Å^3, 54.2% of the crystal volume) led to better refinement and data convergence. Refinement of the structure converged at a final $R_1 = 0.0628$ and $wR_2 = 0.1849$ for 2581 reflections with $I > 2\sigma(I)$; $R_1 = 0.0734$ and $wR_2 = 0.1924$ for all reflections. The largest differences in peak and hole were 0.647 and -0.460 e·Å^{-3}, respectively.

Crystal **2a** was prepared by activating crystal **2** with vacuum-drying at 150 °C overnight. Only one zinc cation and one ligand on the crystallographic mirror plane were observed as an asymmetric unit, and the difference Fourier map did not indicate the presence of any solvent molecules. As in the structure of **2a**, the pyridyl group of the ligand was statistically disordered. All non-hydrogen atoms were refined anisotropically; only the hydrogen atoms attached to the ligand except one hydrogen atom of the statistically disordered pyridyl group were assigned isotropic displacement coefficients U(H) = 1.2U (C) and their coordinates were allowed to ride on their respective atoms. The hydrogen atom of the disordered pyridyl group was not included in the least-squares refinement. The refinement converged to $R_1 = 0.0581$ and $wR_2 = 0.2239$ for 2500 reflections with $I > 2\sigma(I)$; $R_1 = 0.0672$ and $wR_2 = 0.2350$ for all reflections. The largest differences in peak and hole were 1.087 and −0.381 $e \cdot Å^{-3}$, respectively.

A summary of the crystallographic data is given in Table 1. CCDC-735308, 735309, 772329, and 823003 contain the supplementary crystallographic data for **1**, **1a**, **2**, and **2a**, respectively. The data can be obtained free of charge at www.ccdc.cam.ac.uk/conts/retrieving.html or from the Cambridge Crystallographic Data Centre, 12, Union Road, Cambridge CB2 1EZ, UK.

Low-Pressure Gas Sorption Measurements. The N_2 and Ar sorption isotherms for **1a** and **2a** were measured using a BELSORP-max (BEL Japan, Inc.) with a standard volumetric technique up to saturated pressure and the H_2 sorption isotherms for **1a** and **2a** were measured using a BELSORP-mini (BEL Japan, Inc.). The N_2 (with purity of 99.999%) and the Ar (with purity of 99.9999%) sorption isotherms were monitored at 77 and 87 K, respectively. And the H_2 sorption isotherms were measured at both 77 and 87 K. The specific pore volume of the adsorbent was estimated from the adsorption isotherm assuming that the density of the adsorbate in the pore at given temperature and at its saturation pressure is the same as that of the adsorbate in its liquid state at given temperature. The adsorption data in the pressure range lower than ~0.1 P/P_0 were fitted to the Brunauer−Emmett−Teller (BET) equation to determine the BET surface areas. For the Langmuir surface areas, data from the whole adsorption data were used.

High-Pressure Gas Sorption Measurements. The high-pressure H_2 (with high purity of 99.9999%) adsorption experiments for **1a** were conducted by the gravimetric method using a Rubotherm magnetic suspension balance (MSB) apparatus. Approximately 0.2 g of sample was transferred to the sample cell and outgassing was performed overnight at 473 K under a high vacuum. Prior to gas sorption measurement, the helium (99.999%) isotherm (up to 100 bar) was measured at 298 K to obtain the volume of the framework skeleton. The excess-sorption isotherms were measured and the data were corrected for buoyancy by multiplying the volume of the framework skeleton by the density of the corresponding gas at each pressure and temperature.[23] During the sorption measurements, the sample cell was immersed in either a thermostatic bath at 298 K or a cryogenic Dewar at 77 K.

■ RESULTS AND DISCUSSION

We designed a new ligand, H_2L, that has an iph unit for the generation of a paddle-wheel SBU and a pyridyl group interlinked to the iph unit via a C−C triple bond as an auxiliary internal donor group for the fifth coordination site of the metal centers of the paddle-wheel SBU. In addition to a partial flexibility of the iph unit itself,[24] some degree of rotational freedom of the C−C triple bond renders an additional flexibility in the ligand conformation. Introduction of the pyridyl group in the ligand as an auxiliary internal interlinking unit could lead to the construction of a microporous 3-D MOF based on either MOPs interconnected via the pyridyl residues or 2-D layers pillared by the internal pyridyl groups.

A solvohydrothermal reaction of the ligand with $Cu(NO_3)_2 \cdot 2.5H_2O$ in DMF/H_2O in the presence of a small amount of HCl gave the framework **1** and a similar solvothermal reaction with $Zn(NO_3)_2 \cdot 6H_2O$ in DEF in the absence of acid led to the framework **2**.

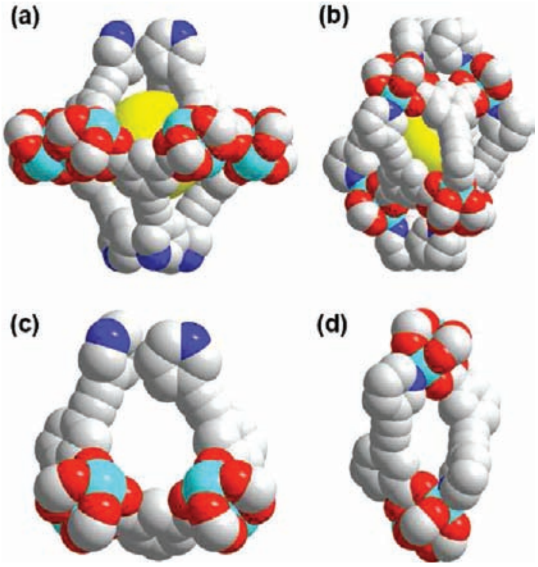

Figure 3. Space-filling models of the cage-like pores; (a) the cage A pores of $[(M_2)_6L_6]$ local composition; (b) the cage B pores of $[(M_2)_6L_6(py)_6]$ local composition; (c) the aperture of the cage A pores; (d) the aperture of the cage B pores. The large yellow balls in the centers of the cages are dummy balls representing the approximate pore dimensions of the cage-like pores.

The single-crystal X-ray diffraction analyses revealed that frameworks **1** and **2** crystallize in different space groups ($R\bar{3}c$ for **1** and $R\bar{3}m$ for **2**); however, the two structures are closely related to each other. The framework with the crystallographic *c*-glide symmetry relationship in the crystal structure of **1** is statistically disordered in the crystal structure of **2** with a reduced *c*-axis dimension. Even though frameworks **1** and **2** are in different space groups, they are isostructural with each other and form the same microporous 3-D MOF having 3-D pores with moderate solvent cavity volumes (54.7% for **1** and 54.2% for **2** of the total crystal volume based on the PLATON calculations) (Figures 1 and S2; Tables 1 and S1). In the frameworks, the iph units are involved in the formation of layered 2-D networks of **kgm** net topology based on the square-planar paddle-wheel SBU, $M_2(COO)_4$ (where M is Cu(II) or Zn(II) ion) (Figure 2a,b). The 2-D layers are undulated and the undulated layers are stacked in a staggered manner, as shown in Figure 2c,d. The stacked layers are interconnected via coordination of the internal pyridyl groups to the fifth coordination site of the metal centers of the paddle-wheel SBUs of the neighboring layers to generate the 3-D MOFs with complicated 3-D solvent cavities (Figure 2e,f).

The pillaring of the internal pyridyl residues between the 2-D layers of **kgm** net topology generates two different types of cages, cage A with $[(M_2)_6L_6]$ local components and cage B with $[(M_2)_6L_6(py)_6]$ local components, where py is the pyridyl part of the ligand (Figures 3 and S3). Arrangement of the components of the cages in different manners leads to two different shapes for the cages. The pore diameters of cages A and B are ~10 Å and ~8.0 Å, respectively. Both of the cages have six apertures of the same shape. However, the shapes and dimensions of the apertures in cage A and cage B are different from each other. Cage A of D_3 symmetry has six approximately circular apertures and

Table 2. The Aperture Dimensions (Å) of the Two Cage-Like Pores, Cage A and Cage B, in the MOFs[a]

cages	aperture distance	1	1a	aperture distance	2	2a
cage A	C4···C11[a]	6.05	6.03	C4···C11[d]	6.22	6.16
	C9[b]···C13	5.50	5.52	C9···C9[e]	5.89	5.85
cage B	O2[c]···O4	**5.85**	**5.88**	O2···O2[f]	**5.93**	**5.93**
	C6···C6[c]	**3.26**	**3.23**	C6···C6[f]	**3.20**	**3.24**

[a] Symmetry codes: (a) $2/3 - x, 1/3 - x + y, 11/6 - z$. (b) $1 - y, 1 + x - y, z$. (c) $-2/3 + y, 2/3 - x - y, 4/3 - z$. (d) $y, x, 2 - z$. (e) $-x + y, y, z$. (f) $1/3 + x - y, 2/3 - y, 4/3 - z$.

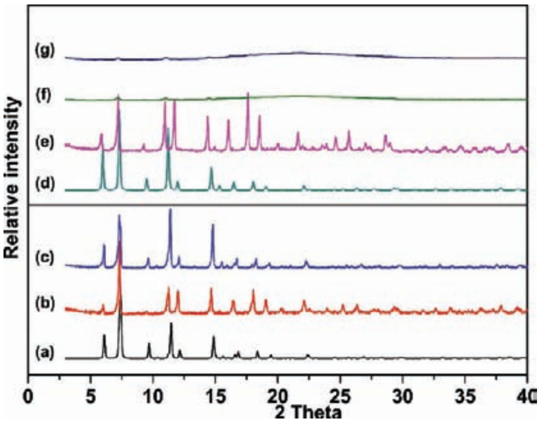

Figure 4. PXRD patterns of **1**, **1a**, **2**, and **2a**. (a) A simulated PXRD pattern from the single-crystal structure of **1**; (b) as-synthesized bulk sample of **1**; (c) **1a**, the sample prepared via soaking **1** in DMF, then vacuum-drying at 200 °C overnight; (d) a simulated PXRD pattern from the single-crystal structure of **2**; (e) as-synthesized bulk sample of **2**; (f) **2a**, the sample prepared via soaking **2** in DEF, then vacuum-drying at 150 °C overnight; (g) **2a**-resolvated, the sample prepared via resolvating the air-exposed **2a** in fresh DEF for 12 h.

the diameter of the aperture is ~6 Å (Table 2). The local symmetry of cage B is also the same D_3 symmetry; however, it has six oval-shaped apertures and the static aperture size is ~3.2 Å in its shortest dimension and ~5.9 Å in its longest dimension (Table 2 and Figure S4).[25] These cages are arranged alternatively in three dimensions and interconnected to each other via channels to form complicated 3-D solvent pores.

The bulk identities and thermal stabilities of the MOFs were characterized by powder X-ray diffraction (PXRD) measurements. A comparison of the simulated PXRD pattern from the single-crystal data of **1** and that for the as-synthesized sample **1** and for the activated sample **1a** indicated that the single crystal is representative of the bulk sample, and the activated sample retained the same structure as that of **1** even after the removal of its solvent molecules in the pores (Figure 4). The single-crystal X-ray diffraction analysis of **1a** also confirmed the stability of the framework. The structure of **1a** is the same as that of **1**; the structural difference is within the experimental error range (Tables 1 and S1).

The thermal stability of **1** has been demonstrated using variable temperature PXRD (VT-PXRD) experiments. The PXRD patterns of the as-synthesized sample up to 375 °C show that the framework is stable at least up to 325 °C (Figure 5a). The hydrothermal stability of **1** has also been demonstrated using samples refluxed in water (Figure 5b). The sample refluxed overnight in water did not indicate any loss of crystallinity. Even the sample was refluxed over 10 days, although some broadenings of the peaks were observed, the main features of the diffraction pattern remained the same as that of the fresh sample.

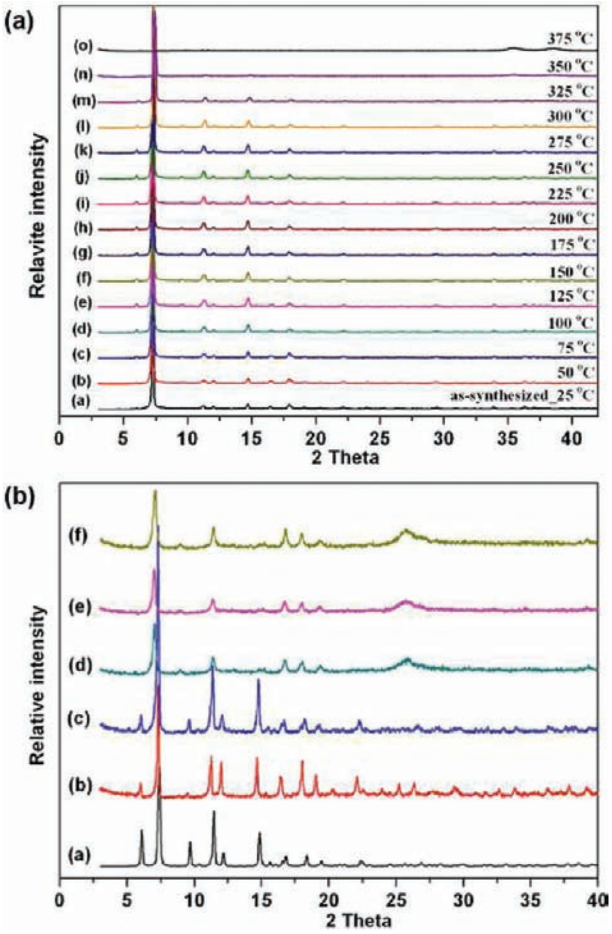

Figure 5. PXRD patterns: (a) VT-PXRD, trace a, as-synthesized, **1** at 25 °C; then heated to trace b: 50 °C; trace c: 75 °C; trace d: 100 °C; trace e: 125 °C; trace f: 150 °C; trace g: 175 °C; trace h: 200 °C; trace i: 225 °C; trace j: 250 °C; trace k: 275 °C; trace l: 300 °C; trace m: 325 °C; trace n: 350 °C; trace o: 375 °C. (b) PXRD patterns of water-treated samples, trace a: simulated pattern from a single-crystal structure of **1**; trace b: as-synthesized, **1**; refluxing compound **1** in water for trace c: overnight; trace d: 1 day; trace e: 2 days; trace f: 10 days.

The PXRD of the as-synthesized **2** indicated that the single crystal of **2** was representative of the bulk sample **2** (PXRD patterns (d) and (e) in Figure 4). The structure of **2a** is the same as that of **2**; the structural difference is within the experimental error range (Tables 1 and S1). In contrast to the hydrothermal stability of **1a**, the activated **2a** is not stable in air. The PXRD of the activated sample exposed to air indicates the loss of its crystallinity (PXRD pattern (f) in Figure 4) and this change is irreversible. The PXRD of the resolvated sample did not indicate any recovery of the crystallinity. The IR spectra of the air-exposed **2a** samples also indicate that **2a** slowly decomposes to some unidentified species in air (Figure S6, Supporting Information).

Because frameworks **1** and **2** have large solvent pores, the desolvated samples **1a** and **2a** (**2a** was prepared by activating the fresh samples at 150 °C under vacuum overnight with no exposure to air) were prepared and their sorption properties were investigated. As shown in Figures 6 and S7, the N_2 sorption isotherm of **1a** at 77 K is type I but shows stepwise adsorption and desorption with no hysteresis, which indicates that there are pores N_2 molecules allowed in only above some threshold pressure, ~0.18 P/P_0, and the framework is quite rigid. The lack of hysteresis during the stepwise sorption of the adsorbate, N_2, around the threshold pressure is related to the rigidity of the framework at the given temperature. While N_2 molecules are allowed into the pores of cage A over the whole pressure range because of the sufficiently large aperture size of the pore, N_2 molecules are allowed into the pores of cage B only above the threshold pressure because the size and shape of the oval-shaped aperture of cage B approximately matches that of N_2 molecules. A small hysteresis at $P/P_0 > 0.50$ (the inset in Figure 6) indicates that the mesoporosity is originated most probably from intercrystalline voids in the sample.[26] The amount of N_2 adsorbed up to the first plateau is ~386 $cm^3\ g^{-1}$, the total amount of N_2 adsorbed in the pores of the framework being 452 $cm^3\ g^{-1}$. The total specific pore volume of **1a** was estimated to be 0.696 $cm^3\ g^{-1}$ based on the total uptake amount of N_2, assuming that the density of N_2 in the pores is the same as that of liquid N_2 at 77 K (d_{N2} = 0.808 g cm^{-3}) (Figure S8, Supporting Information). The pores of cage A and the channel areas interconnecting the two types of cages comprise ~85% of the total pore volume and the pores of cage B comprise the remaining ~15% of the total pore volume. The BET specific surface area calculated using the adsorption data up to the first plateau (P/P_0 range 0.0001−0.0600) is 1560 $m^2\ g^{-1}$, and the BET specific surface area calculated using the adsorption data for the second plateau (P/P_0 range 0.1976−0.2598) is 140 $m^2\ g^{-1}$ (Table 3). The total BET specific surface area (the sum of the two BET specific surface areas) is 1700 $m^2\ g^{-1}$. The Langmuir specific surface area calculated using the whole adsorption data range is 1930 $m^2\ g^{-1}$.

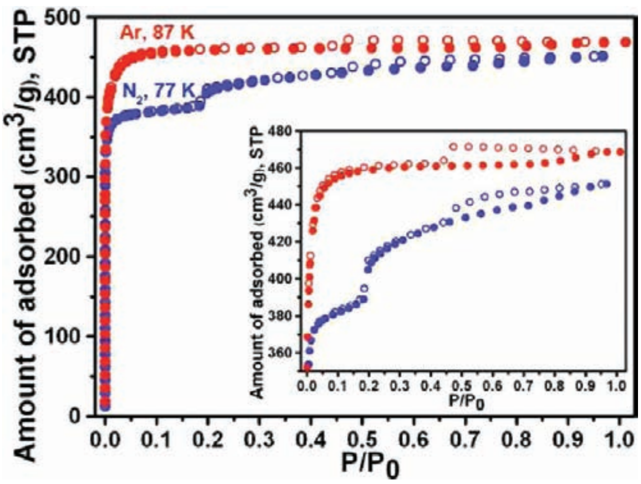

Figure 6. N_2 and Ar sorption isotherms of **1a**. (inset) The expanded isotherms showing a small hysteresis at $P/P_0 > 0.50$. Color codes: N_2 sorption isotherm at 77 K (blue); Ar sorption isotherm at 87 K (red). Filled circles represent the adsorption amounts and open circles represent the desorption amounts.

The Ar sorption isotherm of **1a** at 87 K is also type I with a small hysteresis over the pressure range of 0.5−1.0 P/P_0 (Figures 6 and S7). In contrast to the two-step N_2 adsorption and desorption isotherms, no stepwise behavior was observed in Ar sorption. The BET specific surface area calculated using the adsorption data in the P/P_0 range 0.0008−0.0694 is estimated to be 1620 $m^2\ g^{-1}$, similar to the BET specific surface area obtained using the N_2 adsorption data up to the first plateau in the P/P_0 range 0.0001−0.0600. The Langmuir specific surface area calculated using all of the adsorption data, 1780 $m^2\ g^{-1}$, is 150 $m^2\ g^{-1}$ smaller than the Langmuir specific surface area estimated from the N_2 adsorption isotherm. The total amount of Ar adsorbed into the pores of the framework is ~468 $cm^3\ g^{-1}$. If the density of the Ar in the pores is assumed to be the same as that of liquid Ar at 87 K (d_{Ar} = 1.402 g cm^{-3}), the volume occupied is 0.594 $cm^3\ g^{-1}$, slightly smaller than the total void volume estimated from the N_2 sorption measurement (Figure S8, Supporting Information). This pore volume corresponds to ~85% of the total pore volume, which approximately matches the pore volume of the pores of cage A and the channel areas. Even though the KD of Ar (3.40 Å) is smaller than that of N_2 (3.64 Å),[10b] the analyses of the surface areas and the specific pore volumes based on the N_2 and Ar adsorptions suggest that N_2 with the larger KD is allowed into the pores of cage B above the threshold pressure but Ar with the smaller KD is not. These observations contradict the size-selective sorption behavior of rigid microporous materials for the adsorbates based on their KDs. Shape-dependent parameters such as the MIN-2s[8] determine the

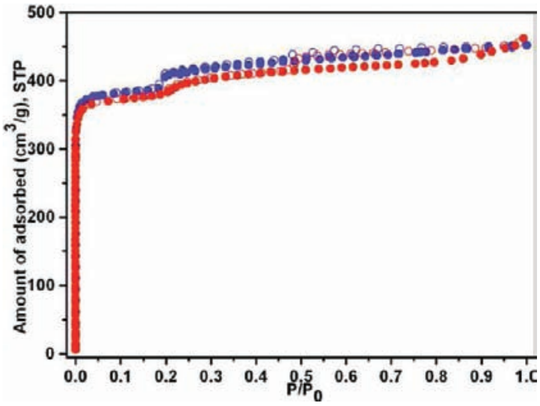

Figure 7. N_2 sorption isotherms on **1a** (blue) and the water-treated sample (red, after refluxing **1** in water overnight, then vacuum-drying at 150 °C overnight) at 77 K.

Table 3. The Specific Surface Areas ($m^2\ g^{-1}$) for 1a and 2a

	1a		2a	
	BET	Langmuir	BET	Langmuir
specific surface areas ($m^2\ g^{-1}$) calculated from N_2 adsorption isotherm	(1560, 140)[a]	1930	1660	1880
specific surface areas ($m^2\ g^{-1}$) calculated from Ar adsorption isotherm	1620	1780	(1560, 320)[a]	1980

[a] The specific surface areas of the pores up to the first plateaus have been calculated using the adsorption data in the $P/P_0 < 0.06$ for both **1a** and **2a**; the specific surface areas of the pores up to the second plateaus have been calculated using the adsorption data in the P/P_0 range of 0.19−0.26 for **1a** and 0.06−0.20 for **2a**, respectively.

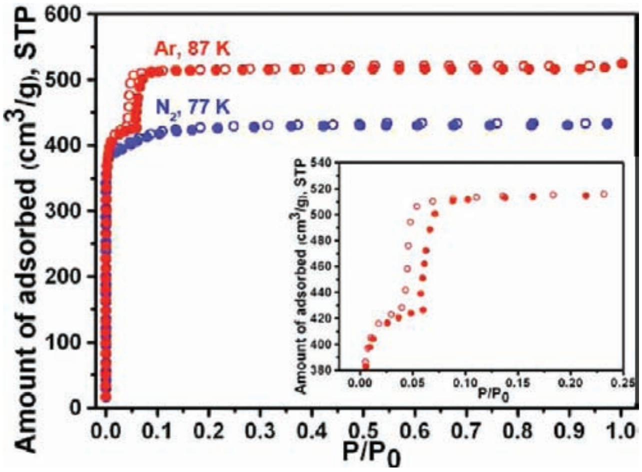

Figure 8. N_2 and Ar sorption isotherms on **2a**. (Inset) The expanded Ar isotherms showing a distinct step at ~0.06 P/P_0 with small hysteresis. Color codes: N_2 sorption isotherm at 77 K (blue); Ar sorption isotherm at 87 K (red). Filled circles represent the adsorption amounts and open circles represent the desorption amounts.

selective sorption behavior. Ar, having a larger MIN-2 value (3.63 Å), is not allowed into the pores of cage B, but N_2 having a smaller MIN-2 value (3.05 Å) is allowed into the pores of cage B. While the combination of the absence of stepwise behavior and the lower total specific pore volume of the Ar sorption isotherms on **1a** indicates that the dimension of Ar is larger than the effective aperture size of cage B of **1a**, the stepwise sorption behavior of N_2 suggests that the dimension of N_2 is comparable to the effective aperture size.

The hydrothermal stability of porous MOFs is one of the most important characteristics for practical applications of MOFs. The high thermal stability of **1** was demonstrated by the VT-PXRD measurements of the as-synthesized **1** (Figure 5a). The PXRD patterns of the water-treated **1a**, where **1** was first activated, refluxed in water, then reactivated by vacuum-drying at 150 °C overnight, also indicated its high hydrothermal stability (Figure 5b). The N_2 sorption isotherm of the water-treated sample, prepared by refluxing the activated **1** in water overnight and then vacuum-drying at 150 °C overnight, shows essentially the same sorption features, two-step adsorption/desorption, and a small hysteresis over the pressure arrange of 0.5−1.0 P/P_0, but with a small decrease in the amount of N_2 adsorbed (Figure 7). This remarkable feature also supports the high hydrothermal stability of **1** not only in regard to the structure but also for properties such as gas sorption.

In contrast to the clear two-step N_2 adsorption isotherm of **1a**, the step in the similar N_2 sorption isotherm of **2a** at 77 K is not clear (Figures 8 and S9). The logarithmic plot of the isotherm shows two gentle steps at the pressures of ~0.005 P/P_0 and of ~0.05 P/P_0. However, the amount of the adsorbate adsorbed even after the first step suggests that the steps are not related to the selectivity of cage B considering the volume of cage B. The BET specific surface area estimated using the adsorption data in the P/P_0 range from 0.0004 to 0.0800 is 1660 $m^2\ g^{-1}$. This BET specific surface area is close to the total BET specific surface area calculated from the N_2 adsorption isotherm obtained with **1a** (Table 3). The Langmuir specific surface area calculated using all of the adsorption data is 1880 $m^2\ g^{-1}$, again similar to the Langmuir specific surface area of **1a**. The amount of N_2 adsorbed in the cavity of the framework is estimated to be 433 $cm^3\ g^{-1}$. The specific pore volume calculated based on the N_2 uptake amount is 0.667 $cm^3\ g^{-1}$ (Figure S10, Supporting Information). Even though the aperture size of the pores of cage B calculated based on the crystal structure **2a** is similar to that based on the crystal structure **1** or **1a** (Table 2 and Figure S4, Supporting Information), the estimated pore volume and the specific surface areas of **2a** strongly suggest that the adsorbate N_2 is not only allowed into the pores of cage A, it is also allowed into the pores of cage B over the whole pressure range, unlike the case of **1a**.

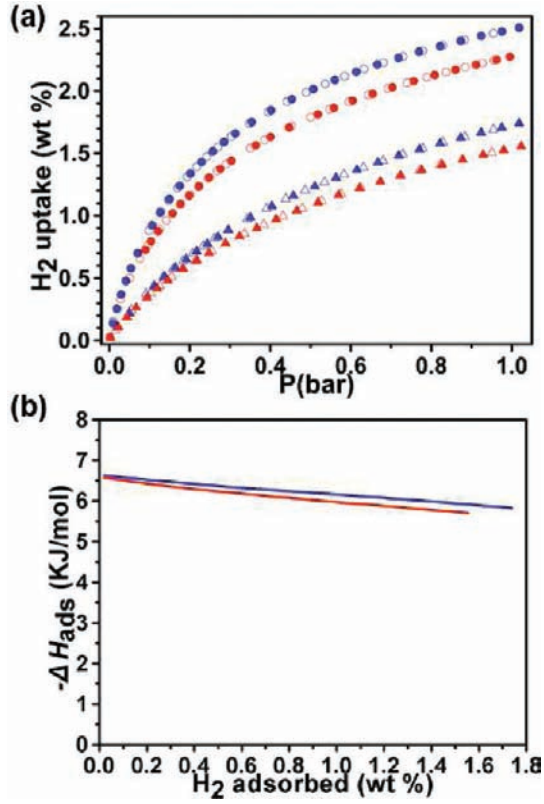

Figure 9. (a) H_2 sorption isotherms on **1a** and **2a** at 77 K (circles) and 87 K (triangles), respectively; (b) H_2 adsorption enthalpies on **1a** and **2a**. Color codes: **1a** (blue), **2a** (red). Filled shapes represent the adsorption amounts and open shapes represent the desorption amounts.

The different selectivities of **1a** and **2a** come from the different flexibilities of the pore apertures in those two structures due to the different extents of thermal vibrations of the frameworks. Even though the static aperture size of the cage B pores in Zn-MOF, **2a**, is similar to that in the isostructural Cu-MOF, **1a**, the effective aperture size of the cage B pores in Zn-MOF is slightly larger than that of the corresponding Cu-MOF, which allows N_2 to access the type B pores of Zn-MOF more easily than for that of Cu-MOF. The larger average thermal factor of the Zn-MOF than that of the Cu-MOF might be responsible for such behavior.[27] The average thermal factor of the atoms constituting the aperture of the cage B pores in the Zn-MOF, **2a**, is about three times of that in the Cu-MOF, **1a** (Table S2, Supporting Information). The size discrimination or the size selectivity of the adsorbents for the adsorbates is not based on the static aperture size of the pores but based on the effective aperture size.

Interestingly, the Ar sorption isotherm of **2a** at 87 K exhibits two distinct steps at ~0.06 P/P_0 with small hysteresis (Figures 8 and S9). The hysteresis indicates the increased flexibility of **2a**

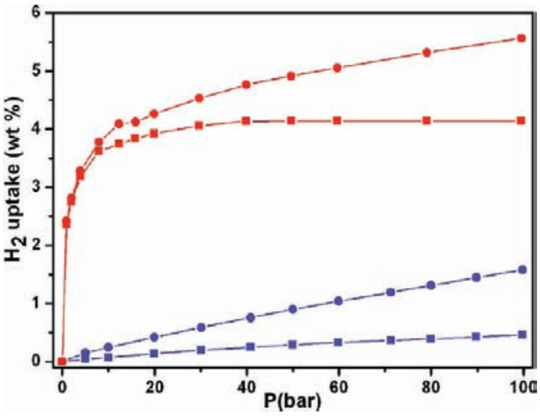

Figure 10. High-pressure H_2 sorption isotherms for **1a**, excess (squares) and total (circles) uptake at 77 K (red) and 298 K (blue).

than **1a**. The amount of Ar adsorbed up to the first plateau is ~430 cm^3 g^{-1}, then a rapid increase of the Ar uptake occurs at ~0.06 P/P_0, and the total uptake amount is ~524 cm^3 g^{-1} at the saturation pressure. The specific pore volume estimated based on the total amount of Ar uptake at 87 K is 0.660 cm^3 g^{-1}, very similar to the specific pore volume estimated based on the total amount of N_2 uptake (Figure S10, Supporting Information). Unlike the case of Ar sorption on **1a**, the Ar adsorbate is allowed not only into the cage A pores of **2a** but also into the cage B pores above the threshold pressure, ~0.06 P/P_0. Again, the larger effective aperture size of the cage B pores of **2a**, caused by the larger thermal motion of the framework of **2a** than that of **1a**, allows the Ar into the cage B pores even though the static aperture size of the cage B pores is not large enough for spherical Ar gas.

The hydrogen sorption isotherms on **1a** and **2a** are given in Figure 9a. The hydrogen uptake of **1a** and **2a** at 77 K and 1 bar was 2.51 wt % and 2.27 wt %, respectively. The adsorption enthalpies were calculated from the H_2 isotherms at 77 and 87 K using the virial method.[28] The isosteric heats of adsorption obtained are in the range 6.63−5.82 kJ mol^{-1} for **1a** (coverage of 0.02−1.74 wt % H_2 uptake) and 6.56−5.69 kJ mol^{-1} for **2a** (coverage of 0.02−1.56 wt % H_2 uptake) depending on the degree of H_2 loading (Figure 9b). The H_2 uptake amount of **1a**, 2.51 wt %, is one of the best for MOFs (2.5−3 wt %).[29] The small pore diameters and the narrow and meandering channel structure of the MOF might be responsible for the relatively high isosteric heats of adsorption despite the lack of so-called unsaturated metal sites for effective adsorbent−adsorbate interaction and is the reason for the high H_2 uptake ability of **1a** at 1 bar and 77 K.

The high-pressure H_2 uptakes on **1a** were measured using a gravimetric method up to 100 bar at 77 and 298 K. The maximum excess H_2 uptakes were 4.14 wt % (at 40 bar) at 77 K and 0.46 wt % (at 100 bar) at 298 K, as shown in Figure 10. The high-pressure hydrogen uptake amounts of **1a** are in the ranges expected from its specific surface area and the isosteric heat of adsorption.[29]

■ CONCLUSIONS

A new iph-based ligand containing a pyridyl unit as an internal auxiliary pillaring linker, 5-(pyridin-3-ylethynyl)isophthalic acid, has been synthesized and used to generate two isostructural microporous 3-D MOFs (Cu-MOF, **1** and Zn-MOF, **2**), where 2-D layers of **kgm** net topology based on the paddle-wheel SBUs were pillared by the internal pyridyl residue to form a 3-D microporous structure. The micropores of the MOFs are composed of two different types of D_3 symmetry cages, with different aperture sizes and shapes, interconnected to form a complicated 3-D channel structure.

While the desolvated Zn-MOF, **2a**, is not stable when exposed to air, the desolvated Cu-MOF, **1a**, is hydrothermally stable in air. The high thermal stability of **1a** has been demonstrated by single-crystal X-ray diffraction analysis and by VT-PXRD. **1a** is even stable under reflux conditions in water.

This study shows that the microporous MOFs can distinguish the adsorbates (N_2/Ar) not based on the widely used KDs of the adsorbates but based on their MIN-2s, which are more shape dependent. While the cage A pores with sufficiently large aperture size compared with the size of the adsorbates do not show any size selectivity, the cage B pores with an approximate size match between the adsorbates and the pore apertures of the MOFs show shape selectivity for the adsorbates. Even though the KD of Ar (3.40 Å) is slightly smaller than that of N_2 (3.64 Å), Ar is not allowed into the cage B pores, whereas N_2 is allowed in. This selectivity is related to the shape match/mismatch between the adsorbate and the pore aperture of the MOFs. The smaller but spherical Ar atom is not allowed into the pores with the oval-shaped aperture, while the larger but linear N_2 molecule is allowed into the pores with the oval-shaped aperture.

Even though **1** and **2** are of the same crystal structure except for the different metal ions at the paddle-wheel SBUs and have the same size of the static apertures, the two MOFs show a different size selectivity on the adsorbates. The different selectivity is based not on the static aperture size of the pore but on the effective aperture size, which reflects the different extent of the framework flexibility. It is not possible to estimate the absolute effective aperture size of the pores from the gas sorption studies; however, the relative effective aperture size could be derived from the stepwise behavior of the sorption isotherms assuming that the effective aperture size of cage B is similar to the dimension of the adsorbate showing stepwise behavior. The effective aperture size of cage B in **1a** is comparable to the dimension of N_2 and that in **2a** is comparable to the dimension of Ar. The Zn-MOF, **2a**, with larger thermal factors around the aperture of the cage B pores behaves as if it has a larger effective aperture size than the Cu-MOF, **1a**, with smaller thermal factors around the aperture of the cage B pores even though both have almost the same static aperture size.

■ ASSOCIATED CONTENT

Ⓢ Supporting Information. Packing diagrams of **1a**, **2**, and **2a**, ball-and-stick views of the two cage-like pores, aperture dimensions of the cage B pores of **1**, **1a**, **2**, and **2a**, IR spectra of **2** and **2a**, TGA data of **1**, **1a**, and **2**, N_2 and Ar sorption isotherms of **1a** and **2a**, and their specific pore volumes occupied by N_2 and Ar, selected bond distances, thermal factors of the aperture constituent atoms, and X-ray crystallographic files (CIF). This material is available free of charge via the Internet at http://pubs.acs.org.

■ AUTHOR INFORMATION

Corresponding Author

*Phone: 82-52-217-2931. Fax: 82-52-217-2019. E-mail: mslah@unist.ac.kr.

■ ACKNOWLEDGMENT

This work was supported by NRF-2010-0019408 and WCU programs (R31-2008-000-20012-0) through the National

Research Foundation of Korea. The authors acknowledge PAL for beamline use (2010-1063-08).

■ REFERENCES

(1) Yang, R. T. *Adsorbents: Fundamentals and Applications*; John Wiley & Sons: Hoboken, 2003.

(2) (a) Mueller, U.; Schubert, M.; Teich, F.; Puetter, H.; Schierle-Arndt, K.; Pastré, J. *J. Mater. Chem.* **2006**, *16*, 626. (b) Couck, S.; Denayer, J. F. M.; Baron, G. V.; Rémy, T.; Gascon, J.; Kapteijn, F. *J. Am. Chem. Soc.* **2009**, *131*, 6326. (c) Matsuda, R.; Kitaura, R.; Kitagawa, S.; Kubota, Y.; Belosludov, R. V.; Kobayashi, T. C.; Sakamoto, H.; Chiba, T.; Takata, M.; Kawazoe, Y.; Mita, Y. *Nature* **2005**, *436*, 238.

(3) (a) Onishi, S.; Ohmori, T.; Ohkubo, T.; Noguchi, H.; Di, L.; Hanzawa, Y.; Kanoh, H.; Kaneko, K. *Appl. Surf. Sci.* **2002**, *196*, 81. (b) Uemura, K.; Matsuda, R.; Kitagawa, S. *J. Solid State Chem.* **2005**, *178*, 2420. (c) Maji, T. K.; Mostafa, G.; Matsuda, R.; Kitagawa, S. *J. Am. Chem. Soc.* **2005**, *127*, 17152. (d) Tanaka, D.; Nakagawa, K.; Higuchi, M.; Horike, S.; Kubota, Y.; Kobayashi, T. C.; Takata, M.; Kitagawa, S. *Angew. Chem., Int. Ed.* **2008**, *47*, 3914. (e) Comotti, A.; Bracco, S.; Sozzani, P.; Horike, S.; Matsuda, R.; Chen, J.; Takata, M.; Kubota, Y.; Kitagawa, S. *J. Am. Chem. Soc.* **2008**, *130*, 13664. (f) Chen, B.; Ma, S.; Zapata, F.; Fronczek, F. R.; Lobkovsky, E. B.; Zhou, H.-C. *Inorg. Chem.* **2007**, *46*, 1233. (g) Seo, J.; Matsuda, R.; Sakamoto, H.; Bonneau, C.; Kitagawa, S. *J. Am. Chem. Soc.* **2009**, *131*, 12792. (h) Li, D.; Kaneko, K. *Chem. Phys. Lett.* **2001**, *335*, 50. (i) Choi, H.-S.; Suh, M. P. *Angew. Chem., Int. Ed.* **2009**, *48*, 6865.

(4) (a) Uemura, K.; Yamasaki, Y.; Komagawa, Y.; Tanaka, K.; Kita, H. *Angew. Chem., Int. Ed.* **2007**, *46*, 6662. (b) Yamada, K.; Tanaka, H.; Yagishita, S.; Adachi, K.; Uemura, T.; Kitagawa, S.; Kawata, S. *Inorg. Chem.* **2006**, *45*, 4322. (c) Kondo, A.; Noguchi, H.; Carlucci, L.; Proserpio, D. M.; Ciani, G.; Kajiro, H.; Ohba, T.; Kanoh, H.; Kaneko, K. *J. Am. Chem. Soc.* **2007**, *129*, 12362. (d) Choi, H. J.; Dincă, M.; Long, J. R. *J. Am. Chem. Soc.* **2008**, *130*, 7848.

(5) (a) Ma, S.; Sun, D.; Wang, X.-S.; Zhou, H.-C. *Angew. Chem., Int. Ed.* **2007**, *46*, 2458. (b) Pan, L.; Parker, B.; Huang, X.; Olson, D. H.; Lee, J. Y.; Li, J. *J. Am. Chem. Soc.* **2006**, *128*, 4180. (c) Mulfort, K. L.; Farha, O. K.; Malliakas, C. D.; Kanatzidis, M. G.; Hupp., J. T. *Chem.—Eur. J.* **2010**, *16*, 276. (d) Zhang, J.-P.; Chen, X.-M. *J. Am. Chem. Soc.* **2008**, *130*, 6010.

(6) (a) Dybtsev, D. N.; Chun, H.; Yoon, S. H.; Kim, D.; Kim, K. *J. Am. Chem. Soc.* **2004**, *126*, 32. (b) Kuznicki, S. M.; Bell, V. A.; Nair, S.; Hillhouse, H. W.; Jacubinas, R. M.; Braunbarth, C. M.; Toby, B. H.; Tsapatsis, M. *Nature* **2001**, *412*, 720. (c) Pan, L.; Adams, K. M.; Hernandez, H. E.; Wang, X.; Zheng, C.; Hattori, Y.; Kaneko, K. *J. Am. Chem. Soc.* **2003**, *125*, 3062. (d) Ma, S.; Wang, X.-S.; Collier, C. D.; Manis, E. S.; Zhou, H.-C. *Inorg. Chem.* **2007**, *46*, 8499. (e) Ma, S.; Wang, X.-S.; Yuan, D.; Zhou, H.-C. *Angew. Chem., Int. Ed.* **2008**, *47*, 4130.

(7) Breck, D. W., *Zeolite Molecular Sieves*; Wiley & Sons: New York, 1974.

(8) (a) Webster, C. E.; Drago, R. S.; Zerner, M. C. *J. Am. Chem. Soc.* **1998**, *120*, 5509. (b) Webster, C. E.; Cottone, A.; Drago, R. S. *J. Am. Chem. Soc.* **1999**, *121*, 12127.

(9) Kim, H.; Samsonenko, D. G.; Yoon, M.; Yoon, J. W.; Hwang, Y. K.; Chang, J.-S.; Kim, K. *Chem. Commun.* **2008**, 4697.

(10) (a) Reference 7, p 65. (b) Reference 7, p 636. Even though the term *effective aperture size* is not mentioned explicitly in ref 10a, the aperture size dependence on the thermal vibration of the aperture constituting atoms has been discussed.

(11) (a) Eddaoudi, M.; Kim, J.; Wachter, J. B.; Chae, H. K.; O'Keeffe, M.; Yaghi, O. M. *J. Am. Chem. Soc.* **2001**, *123*, 4368. (b) Furukawa, H.; Kim, J.; Ockwig, N. W.; O'Keeffe, M.; Yaghi, O. M. *J. Am. Chem. Soc.* **2008**, *130*, 11650. (c) Abourahma, H.; Coleman, A. W.; Moulton, B.; Rather, B.; Shahgaldian, P.; Zaworotko, M. J. *Chem. Commun.* **2001**, 2380. (d) Jung, M.; Kim, H.; Baek, K.; Kim, K. *Angew. Chem., Int. Ed.* **2008**, *47*, 5755.

(12) (a) Bourne, S. A.; Lu, J.; Mondal, A.; Moulton, B.; Zaworotko, M. J. *Angew. Chem., Int. Ed.* **2001**, *40*, 2111. (b) Gao, L.; Zhao, B.; Li, G.; Shi, Z.; Feng, S. *Inorg. Chem. Commun.* **2003**, *6*, 1249.

(13) (a) Moulton, B.; Lu, J.; Hajndl, R.; Hariharan, S.; Zaworotko, M. J. *Angew. Chem., Int. Ed.* **2002**, *41*, 2821. (b) Ma, S.; Sun, D.; Yuan, D.; Wang, X.-S.; Zhou, H.-C. *J. Am. Chem. Soc.* **2009**, *131*, 6445. (c) Perry, J. J.; McManus, G. J.; Zaworotko, M. J. *Chem. Commun.* **2004**, 2534.

(14) Chun, H. *J. Am. Chem. Soc.* **2008**, *130*, 800.

(15) (a) Dybtsev, D. N.; Chun, H.; Kim, K. *Angew. Chem., Int. Ed.* **2004**, *43*, 5033. (b) Chun, H.; Dybtsev, D. N.; Kim, H.; Kim, K. *Chem.—Eur. J.* **2005**, *11*, 3521. (c) Ma, B.-Q.; Mulfort, K. L.; Hupp, J. T. *Inorg. Chem.* **2005**, *44*, 4912. (d) Bae, Y.-S.; Mulfort, K. L.; Frost, H.; Ryan, P.; Punnathanam, S.; Broadbelt, L. J.; Hupp, J. T.; Snurr, R. Q. *Langmuir* **2008**, *24*, 8592. (e) Chen, B.; Ma, S.; Zapata, F.; Lobkovsky, E. B.; Yang, J. *Inorg. Chem.* **2006**, *45*, 5718. (f) Yue, Q.; Sun, Q.; Cheng, A.-L.; Gao, E.-Q. *Cryst. Growth Des.* **2010**, *10*, 44.

(16) (a) Zhang, S.-M.; Chang, Z.; Hu, T.-L.; Bu, X.-H. *Inorg. Chem.* **2010**, *49*, 11581. (b) Xiang, S.; Huang, J.; Li, L.; Zhang, J.; Jiang, L.; Kuang, X.; Su., C.-Y. *Inorg. Chem.* **2011**, *50*, 1743.

(17) *Materials Studio program*, version 4.3; Accelrys: San Diego, CA, 2008.

(18) Arvai, A. J.; Nielsen, C. *ADSC Quantum-210 ADX Program*; Area Detector System Corporation: Poway, CA, USA, 1983.

(19) Otwinowski, Z.; Minor, W. In *Methods in Enzymology*Carter, Jr., C. W.; Sweet, R. M., Ed.; Academic Press: New York, 1997; 276, part A, pp 307–326.

(20) Rapid Auto software, version 2.40; Rigaku Corporation: Tokyo, Japan.

(21) Sheldrick, G. M. *SHELXTL–PLUS, Crystal Structure Analysis Package*; Bruker Analytical X-ray: Madison, WI, 1997.

(22) PLATON program: Spek, A. L. *Acta Crystallogr., Sect. A* **1990**, *46*, 194.

(23) NIST chemistry webbook (thermophysical properties of fluid systems); http://webbook.nist.gov/chemistry/fluid.

(24) Zhang, Z.; Wojtas, L.; Zaworotko, M. J. *Cryst. Growth Des.* 2011, *11*, 1441–1445.

(25) Depending on the stacking pattern of the disordered pyridyl groups along the crystallographic *c*-axis, the cage B in the framework **2** could have three different apertures. However, the stacking disorder is not directly affecting the largest aperture dimensions because they are determined based on the distance between the symmetry related C6 carbon atoms and the distance between the symmetry related O2 oxygen atoms as shown in Figure S5 (also see Table 2).

(26) (a) Vishnyakov, A.; Ravikovitch, P. I.; Neimark, A. V.; Bulow, M.; Wang, Q. M. *Nano Lett.* **2003**, 3, 713. (b) Lee, J. Y.; Li, J.; Jagiello, J. *J. Solid State Chem.* **2005**, *178*, 2527. (c) Moon, H. R.; Kobayashi, N.; Suh, M. P. *Inorg. Chem.* **2006**, *45*, 8672.

(27) We cannot ignore the possibility that the different extents of the average thermal factors in the two MOFs are not the result of the different inherent flexibilities in the MOFs, **1a** and **2a**, but of the different characteristics of the individual single crystals, such as the different mosaicity of the individual crystals. The stacking disorder of the pyridyl groups along the *c*-axis in **2** could also be the reason for the larger average thermal factor in **2a** than that in **1a**.

(28) (a) Cole, J. H.; Everett, D. H.; Marshall, C. T.; Paniego, A. R.; Powl, J. C.; Rodriguez-Reinoso, F. *J. Chem. Soc., Faraday Trans.* **1974**, *70*, 2154. (b) O'Koye, I. P.; Benham, M.; Thomas, K. M. *Langmuir* **1997**, *13*, 4054. (c) Reid, C. R.; O'Koye, I. P.; Thomas, K. M. *Langmuir* **1998**, *14*, 2415. (d) Reid, C. R.; Thomas, K. M. *Langmuir* **1999**, *15*, 3206.

(29) (a) Ma, S.; Zhou, H.-C. *Chem. Commun.* **2010**, *46*, 44. (b) Zhao, D.; Yuan, D.; Zhou, H.-C. *Energy Environ. Sci.* **2008**, *1*, 222.